

Exploring Aluminum-Antimony Intermetallic Chemistry for High-Capacity Cheap and Scalable Battery

Ayan Dey, Sougata Halder, Ghanshyam Varshney, Andrews Cyril A, Ankit Dev Singh, Amitava Banerjee,* and Srijan Sengupta*

Rechargeable aluminum batteries have sparked immense interest as one of the future energy storage devices owing to safer chemistry, abundance of raw materials, and scalability at a much cheaper price than lithium-ion batteries. However, the difficulty of inserting Al^{3+} ions in the positive electrode is still the bottleneck in commercializing this battery technology. To avoid this failure due to intercalation, this work has come up with an alternative solution in which an intermetallic battery with Al as anode and Sb as cathode has been fabricated. During discharge, Al spontaneously forms AlSb intermetallic, delivering energy, and during charge, Al gets electroplated back. Ni-foam has been used as the current collector,

leveraging its 3D-microporous structure to support Sb and significantly reduce capacity decay, without any modification in the current collector or in the separator. This Sb electrode deposited on microporous Ni-foam showcased a stable electrochemical performance, delivering 81 mAh g^{-1} at a current density of 100 mA g^{-1} . Through theoretical simulation (density functional theory), the experimental finding has been further validated to establish the intermetallic chemistry. These compelling results lead the way for the development of an intermetallic chemistry battery for future-generation Al-based batteries.

1. Introduction

Global warming has become a major concern throughout the world as the use of excessive fossil fuels causes serious environmental pollution. There are several energy storage devices that have been around, such as rechargeable batteries,^[1–3] fuel cells^[4] and supercapacitors.^[5] Among them, Li-ion batteries^[6–9] have drawn significant attention due to their unique features, like higher energy density and longer life cycle. These unique features are helpful in the portable electronics field and, to some extent, electric vehicles. Despite such advantages, for large-scale storage applications, the use of Li-ion batteries is still arguable, as in the Earth's crust, the resource of lithium is limited.^[10]

On the contrary, Al is an abundant metal^[11] present in the crust of the earth, which is largely distributed in countries such as Guinea, Australia, Vietnam, Brazil, Jamaica, and India.

Therefore, these countries must look forward to constructing a battery based on Al-chemistry, which offers safer chemistry, is cheap, available, is scalable, and reduces dependency on Li-chemistry for large-scale storage.

Aluminum-ion batteries,^[12–15] are a class of rechargeable batteries that have trivalent charge carriers, that is, Al^{3+} . Therefore, the insertion of one Al^{3+} is similar to three Li^+ ions. Therefore, the insertion of one Al^{3+} is equivalent to three Li^+ ions. Since the ionic radii of Al^{3+} (0.54 \AA) and Li^+ (0.76 \AA) are almost the same, notably higher numbers of electrons and Al^{3+} ions can be acquired by cathodes with some damage. However, the trivalent charge carrier, Al^{3+} , has both the merits and demerits of this type of battery. However, this trivalent charge carrier helps to enhance the theoretical specific capacity while transferring 3 electrons at a time.^[16] The electrostatic intercalation of the electrodes with a trivalent cation is too strong for unambiguous electrochemical activity. The Coulombic interaction between the high charge density Al^{3+} and the electrode host lattice provides a route to poor kinetics and inadequate cycle life. Metal chalcogenides and oxides, sulfides, have poor rate capacity and cycling stability.^[17–20]

To mitigate this problem, this work has come up with an idea of an intermetallic battery chemistry based on Al. In this Al-based intermetallic battery, Al will function as the negative electrode, and Sb will act as the positive electrode with eutectic [EMIm]Cl-AlCl₃, room temperature ionic salt, as the electrolyte.^[21–25] During discharge, Aluminum forms AlSb intermetallic with Sb with a specific capacity of 81 Ah Kg^{-1} and a specific energy of 38 Wh Kg^{-1} , and during charge, aluminum (Al) gets plated back in the negative electrode. Nickel-foam (Ni-foam), owing to its 3D-microporous structure, has been used as the current collector (with Sb) to accommodate the large volume expansion^[26] during discharging and formation of AlSb intermetallic. Density

A. Dey, S. Halder, G. Varshney, A. C. A, A. D. Singh, A. Banerjee, S. Sengupta

Department of Metallurgical and Materials Engineering

Indian Institute of Technology Jodhpur

Rajasthan 342030, India

E-mail: amitava@iitj.ac.in

srijansengupta@iitj.ac.in

A. Banerjee

Inter-disciplinary Research Platform (IDRP) -Space Science Technology

Indian Institute of Technology Jodhpur

Rajasthan 342030, India

S. Sengupta

Rishabh Centre for Research and Innovation in Clean Energy

Indian Institute of Technology Jodhpur

Rajasthan 342030, India



Supporting information for this article is available on the WWW under <https://doi.org/10.1002/batt.202500513>

functional theory (DFT) has been implemented for an atomistic study, providing insights into charge storage, ion transportation paths, and the formation energy required for the intermetallic during the electrochemical process, as well as the charge storage mechanism^[27] of the Al-based batteries. This work aims to conclusively demonstrate the underlying mechanisms of the Al-Sb batteries through their intermetallic formation, a combination of atomistic study and experimental findings.

2. Proposed Strategy

The idea of an Al-based intermetallic battery can be drawn from the Li-ion battery itself. Li-ion battery's working principle is based on the intercalation mechanism, where the cell's potential is a function of state of charge. Therefore, any new material is first tested under a half-cell configuration with Li as the reference electrode. In recent times, conversion-type metallic electrodes such as Sn^[28] Sb,^[29] Pb,^[30] Bi,^[31] and so on. have emerged as a replacement for graphite owing to their high volumetric specific capacity. When tested under a half-cell configuration, these metals form intermetallics during discharge and revert back to pristine metallic form while charging.

However, this idea of intermetallic can be deployed for aluminum as dendrite-free electrodeposition of aluminum from [EMIm]Cl-AlCl₃ baths has been reported. During discharge, aluminum forms AlSb intermetallic, and during charge, Al gets plated back in the negative electrode (**Figure 1**). The charging-discharging reaction involves the migration of Al³⁺ ions towards the cathode, forming an intermetallic, and then again comes back during charging.

The regular Copper (Cu) current collector has been replaced by a Ni-foam. This 3D porous interconnected Ni scaffold helps to accommodate the volume expansion/contraction during the discharging-charging cycles. **Figure 2** shows the porous interconnected structure, which also helps to bind the Sb during the electrodeposition. Further, Sb can be directly electrodeposited on Ni foam, without the help of any binder or conducting agents.

3. Experimental Section

3.1. Electrochemical Fabrication of the Sb Electrode on Ni-Foam

Sb was electrodeposited on the battery-grade Ni-foam current collector from a bath consisting of tartaric acid (Sigma Aldrich, >99.5%) and 1 M SbCl₂ (Alfa Aesar, ≈200 mesh size). Potentiostatic electrodeposition was carried out in Wave Driver 100 (Pine Research, USA) with a rectangular-shaped battery-grade Ni-foam as a current collector and platinum as a counter electrode (area 1 cm²) in a standard two-electrode system at 25 °C. The deposition was carried out at an overpotential of 5 V for 300 s without any mechanical stirring. The as-prepared electrodeposited electrodes were kept inside a vacuum oven at 80 °C for 24 h to eliminate any trace of electrolyte solution.

3.2. Structural Characterization

The as-prepared electrodes were characterized by using an X-ray diffractometer (XRD) to ensure their phase composition. The XRD pattern of the pristine and cycled electrode was obtained using a Bruker D8 Advance diffractometer (using Cu-K α radiation, $\lambda = 1.5406 \text{ \AA}$) and analyzed using Xpert High-score Plus (Malvern Pan-analytical) Software. To investigate the morphology of the pristine and cycled electrode, SEM (scanning electron microscope) (Zeiss Evo 18 and Thermo Fisher Scientific Apreo 2 S) images were collected. Furthermore, to ensure the elemental composition of the electrode, energy-dispersive X-ray spectrometry (EDS) with SEM was performed on the electrode.

3.3. Computational Details

The DFT calculations were conducted using the Perdew–Burke–Ernzerhof (PBE) parameterization of the generalized gradient approximation and the projector-augmented-wave (PAW)^[32] basis

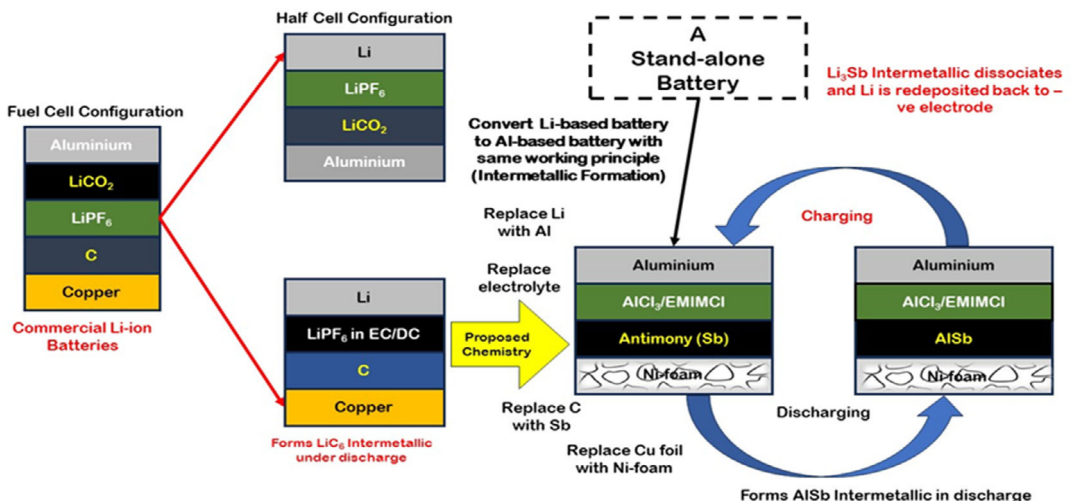


Figure 1. Working principle of the proposed aluminum-antimony intermetallic battery.

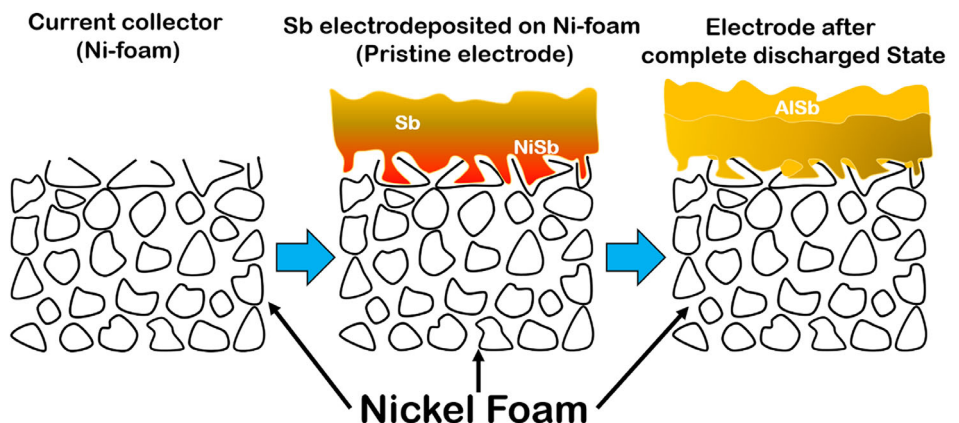


Figure 2. Ni-foam as the current collector with proposed intermetallic formation chemistry.

in the Vienna Ab initio Simulation Package code.^[32] The calculations included spherical and nonspherical contributions to the gradient corrections inside the PAW spheres. Valence electrons were illustrated using a plane wave basis set with an energy cutoff of 520 eV. The structural optimization was carried out using the conjugate-gradient algorithm with a convergence criterion of 10^{-4} eV/cell for energy and 0.001 eV \AA^{-1} for the Hermann-Feynman force. The Monk-Horst-Pack scheme of $8 \times 8 \times 8$ was used to sample the Brillouin zone for the structural optimizations.^[33] Spin polarization, full relaxation of atomic positions, cell shape, and cell volume were considered for all calculations. The Bader charge approach was applied to gain a deep understanding of the charge distribution and transfer.^[33] For investigating the ionic transport properties, the climbing nudged elastic band (cNEB)^[34,35] method was used to calculate the migration energy of Al in the cathode. In this investigation, a supercell containing 32 formula units was employed, and a $4 \times 4 \times 4$ Monkhorst-Pack scheme of k-mesh was used owing to the large size of the supercell. The activation energies were determined using the cNEB framework, and 3 or 5 images were linearly interpolated between the two equilibrium sites for each considered migration path. Geometries assembled when forces on every atom were less than 2 meV \AA^{-1} .

3.4. Electrolyte Design

The AlCl_3 (Anhydrous, Sigma Aldrich) and [EMIm]Cl (Sigma Aldrich) were used to fabricate the electrolyte. The electrolyte was prepared inside an argon-filled glovebox (O_2 ppm < 1.0) by mixing the AlCl_3 and [EMIm]Cl in the molar ratio of 1.3:1. The obtained solution was stirred for 30 min, resulting in a transparent room-temperature ionic liquid, which was used as an electrolyte.

3.5. Coin-Cell Fabrication and Electrochemical Characterization

The electrochemical performance of the electrodeposited Sb electrode on the Ni-foam current collector was tested by assembling it as a CR2032-type coin cell in half-cell configuration. An electrodeposited Sb electrode is punched into a 15 mm diameter circular disk via a manual punching machine (Gelon GN-CP20) to be used as a positive electrode. Al foil was mechanically washed via emery paper to remove the oxide layer on it, then it was also cut into a 15 mm circular disk form to use as an anode. Porous Celgard 2400 was used as a separator that was soaked in

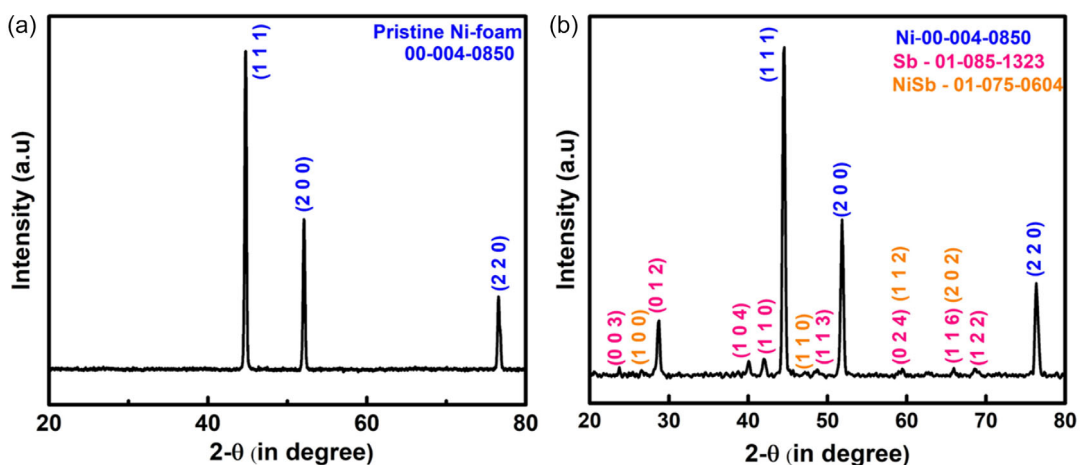


Figure 3. XRD spectra of a) pristine ni-foam and b) electrodeposited sb on ni-foam current-collector.

electrolyte. It obstructs the transportation of electrons between the cathode and the anode. Room temperature-based ionic salt AlCl_3 /[EMIm]Cl was used as an electrolyte. To fabricate the CR2032 type of coin cell, cathode, anode, and separator have been crimped together with the help of a manual crimping machine (Gelon GNCC-20) that is being kept inside the argon-filled, moisture- and oxygen-controlled ($<0.1 \text{ ppm}$) glovebox (Prores Scientific Prolab GB II). The galvanostatic charge-discharge profile was investigated via the automated battery tester (Neware BTS 4000) at room temperature within the voltage range of 0.02–1.8 V. The rate capability test was performed with a step-wise increment in discharge rate from 100 mAg^{-1} to 300 mAg^{-1} .

4. Results and Discussions

4.1. Structural Characterization of the Electrodeposited Sb Electrode

Figure 3a,b show the X-ray diffraction pattern of the pristine Ni-foam and electrodeposited Sb on Ni-foam, respectively. The XRD pattern shows several different diffraction peaks in the range of 20° – 80° . Here, the Ni-foam (00-004-0850) is taken as a reference that shows the peaks at 44.49° , 51.87° , and 76.38° corresponding to the (111), (200), and (220) planes, respectively. In the case of electrodeposited Sb on Ni-foam, Sb (01-085-1322), NiSb (00-041-1439), and Ni (00-004-0850) phases are found to be present. For the Sb phase, the diffraction peaks at 23.75° , 28.75° , 40.05° , 42.05° , 48.75° , and 68.55° correspond to the (003), (012), (104), (110), (113), and (222) planes, respectively. For the NiSb phase, peaks are found at 26.55° , 47.15° , 59.45° , and 65.95° , corresponding to the (100), (110), (112), and (202) planes, respectively. Ni peaks

are also present, as it is used as the current collectors. As no other residue diffraction peaks are observed, this strongly suggests the purity of Sb deposition on bare Ni-foam used as the current collector.

4.2. Morphological Analysis of Electrodeposited Sb Electrode

To investigate the morphology of the electrodeposited working electrode (Sb on Ni-foam current collector), SEM images were taken. Figure 4a-d show the SEM images of the pristine Ni-foam and electrodeposited Sb at magnifications of 100x and 500x, respectively. The pristine Ni-foam shows 3D microporous structures, attributing a much higher surface area. It is observed that the deposition of Sb is uniform and planar over the Ni-foam electrode. The morphology of deposited Sb was planar after completely filling the pores of the Ni-foam. The porous 3D interconnected structure of Ni-foam favors the faster diffusion of Al^{3+} ions, and additionally, it provides more breathing spaces to buffer the volume expansion during the intermetallic formation. Figure 4e (inset) shows the EDS elemental mapping of the electrodeposited Sb on Ni-foam, corresponding to Figure 4d, which shows the weight percentage of Sb and Ni as 43.10 and 56.90%, respectively. This confirms the deposition of Sb over the Ni-foam current collector without any impurity.

4.3. Electrochemical Study of Al-Sb Intermetallic Chemistry

The galvanostatic charge–discharge profile of the electrodeposited Sb electrode is shown in Figure 5a between the potential range of 0.02–1.8 V versus $\text{Al}/\text{AlCl}_4^-$. The electrodeposited Sb electrode shows the first discharge capacity of 81 mAh g^{-1} and the second discharge capacity of 74 mAh g^{-1} , respectively,

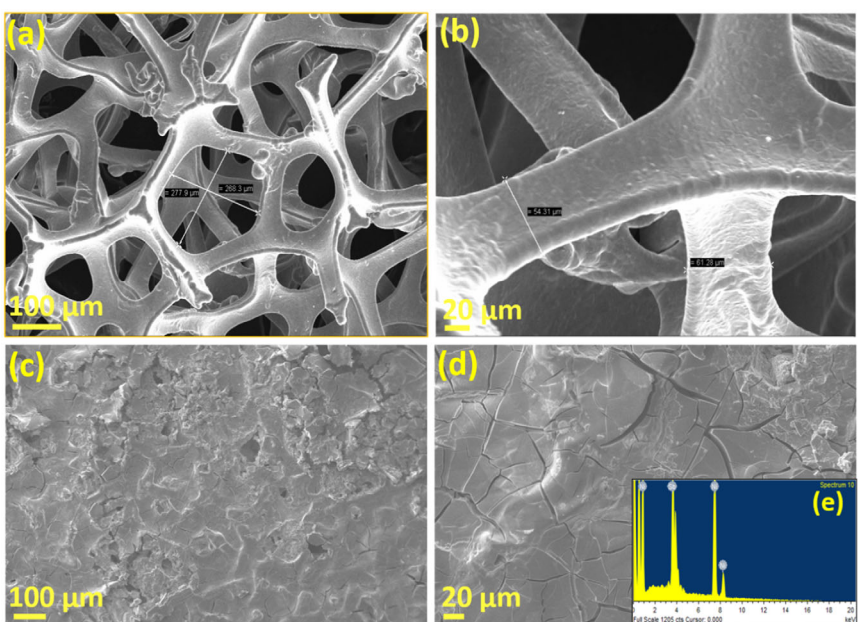


Figure 4. SEM images of a,b) bare ni-foam and c,d) electrodeposited sb on ni-foam current collector at 100x and 500x magnification, respectively; e) EDS of the electrodeposited sb (inset).

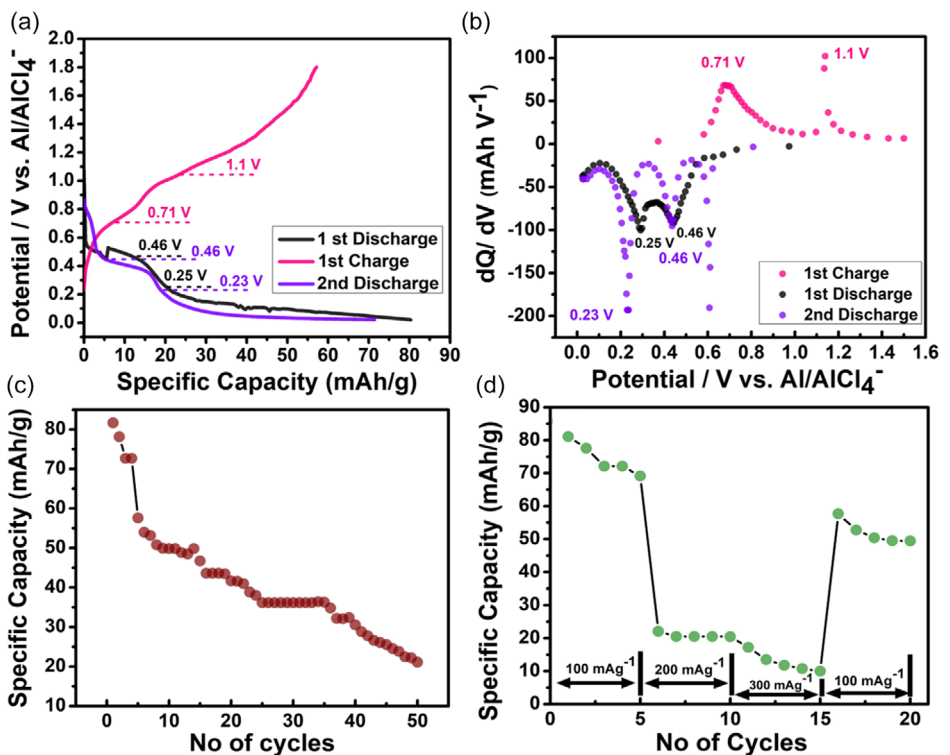
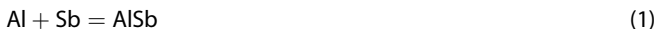


Figure 5. a) charge/Discharge profiles of sb electrode at 100 mAg^{-1} , b) differential capacity versus voltage Profile, c) cyclability of Sb electrode at a current density of 100 mAg^{-1} , and d) rate Capability of Sb electrode at current densities of $100, 200$, and 300 mAg^{-1} , respectively.

at a current density of 100 mAg^{-1} . From the discharge profile, two plateaus were found at around 0.25 V and 0.46 V versus $\text{Al}/\text{AlCl}_4^-$. The plateau at 0.46 V is attributed to the formation of AlSb intermetallic from pure Sb (Equation 1). The intermetallic formed during the discharge process is confirmed by the formation energy calculated through DFT and posttesting XRD studies, as discussed in section 4.4 and 4.5, respectively.



During the discharge process, the Sb phase reacts with Al, forming AlSb and inactive Ni, which acts as a buffer to volumetric expansion. In the charge profile, two peaks are observed at 0.71 V and 1.2 V , which shows the reversibility of (Equation 1) that is, the reversibility of the formation of the AlSb intermetallic phase. The formation of the phases at each redox peak is discussed in section 4.5 (DFT analysis). The formation of the AlSb intermetallic phase has been verified by the XRD at the discharged state (Figure 6) elaborated under section 4.4. DFT analysis under section 4.5 also indicates the formation of the AlSb phase during the discharge process. This reversible formation of AlSb helps to gain the capacity.

The cyclic performance of the electrodeposited Sb electrode for 50 cycles at a current density of 100 mAg^{-1} is shown in Figure 5c. The electrode shows a first discharge capacity of 81 mAh g^{-1} , and a second discharge capacity shows 74 mAh mg^{-1} . The full cell shows a slight drop in capacity during the initial 4 cycles, with a fifth cycle discharge capacity of 58 mAh g^{-1} .

From the fifth cycle onwards, the cell shows a gradual decrease in capacity while retaining around 28% of its initial cycle capacity after 50 cycles. In this study, Ni-foam is used as the current collector for the Sb electrode to impart mechanical stability. The electrode shows a high initial capacity of 81 mAh g^{-1} without any modification. The superior performance of this electrodeposited Sb electrode can be associated with enhanced mechanical stability due to the 3D-interconnected structure of the Ni-foam current collector that provides breathing space during the volumetric expansion and enhancement of interface bonding between the Ni-foam current collector and Sb electrode. This current collector also helps to lower the dissolution of active material (Sb). DFT study (as discussed under section 4.5) further supports the mechanical stability of the Sb electrode when combined with the Ni-foam current collector. This Ni-foam's (current collector) mechanical integrity gives better retention of capacity rather than any modification of the separator or the electrode.

The rate capability test of the electrodeposited Sb electrode over Ni-foam current collector was conducted at the current density between 100 mAg^{-1} to 300 mAg^{-1} , and the average discharge capacity was found to be 74.6 mAh g^{-1} . On increasing the current density to 200 and 300 mAg^{-1} , the average specific capacity decreases to 17.2 mAh g^{-1} . On reintroducing the current density of 100 mAg^{-1} , the electrodeposited Sb electrode shows an average specific capacity of 52.3 mAh g^{-1} , which is 71% of the initial average capacity. This indicates a good rate performance rather than the use of a modified separator or electrode (protection coating). This high reversibility in specific capacity can be

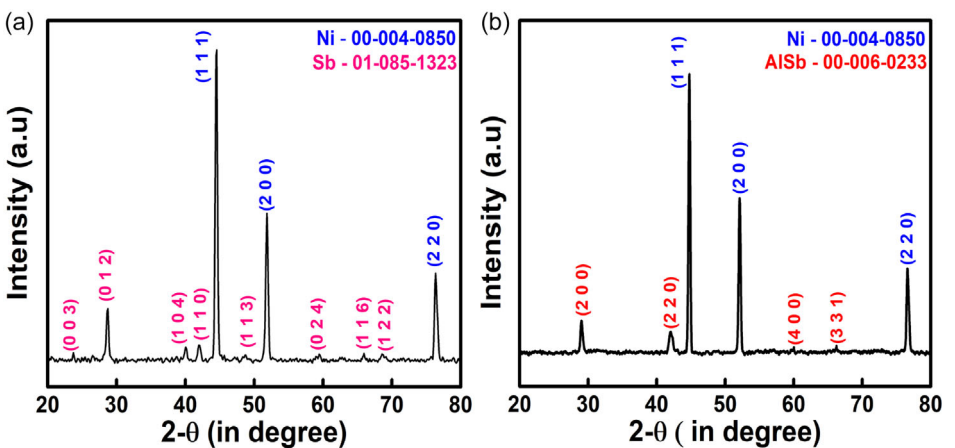


Figure 6. XRD spectra of a) pristine positive electrode (Sb electrodeposited) on Ni-foam current collector and b) at the fully discharged state, respectively.

attributed to the superior structural and mechanical integrity due to the presence of Ni-foam current collector, which helps to provide volume expansion during the charging–discharging cycle.

4.4. Ex Situ XRD Study of the Sb Electrode at the Fully Discharged State

To further understand the intermetallic chemistry mechanism, the XRD spectra of pristine and fully discharged (0.02 V vs. Al/AlCl₄⁻) state of the working electrode (Sb) have been taken, as shown in the Figure 6a,b respectively. Also, a detailed XRD study and analysis have been done to identify the redox peaks for each redox potential, which is shown in the Figure S3, Supporting Information. The XRD spectra of the pristine electrode (Figure 6a) show the presence of Ni and Sb as discussed in section 4.1. In the fully discharged state (at 0.02 V), XRD spectra after 50 cycles, Ni (00-004-0850), and AISb (00-006-0233) phases are present. The XRD spectra of the fully discharged electrode (Figure 6b) show peaks of AISb in addition to the peaks of Ni. The formation of the intermetallic AISb phase during the discharge step is as expected due to the reaction between Al and Sb to form the intermetallic AISb phase around 0.45 V versus Al/AlCl₄⁻ (further confirmed by DFT under section 4.5). The discharge spectra show the peaks of AISb at 29.02°, 41.98°, 60.02°, and 66.24° corresponding to the (200), (220), (400), and (331) planes, respectively. The peaks for the Ni phase were observed from the Ni-foam current collector.

4.5. Theoretical Framework of Intermetallic Mechanisms (DFT Analysis)

The DFT-based atomistic study was used to understand the reaction mechanism of intermetallic compounds and corresponding changes in the cathode structure during the charging cycle. During the discharging cycle, aluminum comes into the cathode and forms the intermetallic AISb. The calculated formation energy of the AISb phase (space group Fm-3m) with reference to Al (space group m-3m) and Sb (space group R-3m) is -0.34 eV, suggesting the feasibility of the formation of this intermetallic phase in the

cathode during the discharging process. A similar phase has been observed in the XRD. Bader charge analysis of the AISb phase suggests that the Al loses a charge of 1.576e⁻, and a similar amount of charge is gained by Sb. The charge density of the (110) plane of the AISb phase also confirms the same, as shown in Figure 7b. Formation energy of NiSb phase is -0.54 eV with respect to per formula unit of Ni and Sb bulk-phase, which also suggests thermodynamic feasibility of NiSb formation. Migration of the active element in the host electrode plays a significant role in the battery performance. Two possible pathways have been considered symmetrically to understand the Al migration. Additionally, occupancy at high-symmetry sites helps to reduce lattice scattering, thereby lowering the resistance in the charge transport process and improving charge transport efficiency. Al migration along the b-direction shows the smallest barrier of 0.96 eV compared to a very large barrier in the other pathway, suggesting one of the most possible pathways of Al migration in the AISb during the charge–discharge cycle. The volume change of the electrode during the charge–discharge cycle could cause capacity decay along with delamination. Here, we have considered the charging cycle to understand the change in the volume of the cathode. To understand the systematic change of the volume with the removal of Al, we have considered another phase, Al0.5 Sb. Although the formation energy (0.26 eV) of this phase suggests that the phase will not form, that's why it was not observed in the experiment. Figure 7a shows the volume contraction of 30% due to the removal of half of the Al from the AISb, and 60% more contraction in the removal of all Al from the cathode. In Figure 7a, the Sb cathode has a different crystal structure compared to the considered reference phase of Sb in the formation energy calculation. It is also observed that the generated Sb phase after Al removal is higher in energy compared to the considered reference phase of Sb. This means that in the end, the generated Sb phase could transform into the thermodynamically stable phase.

DFT computed an average equilibrium voltage of 0.11 V for the alloying step referenced to bulk Al and Sb ($Sb + Al \rightarrow Al/Sb$) by considering the equation: $V_{DFT} = \frac{E(AlSb) - E(sb) - E(Al)}{3e}$. This is suggesting alloying is thermodynamically allowed at low potential. At 0K solid-state reaction energy for the associated displacement exchange

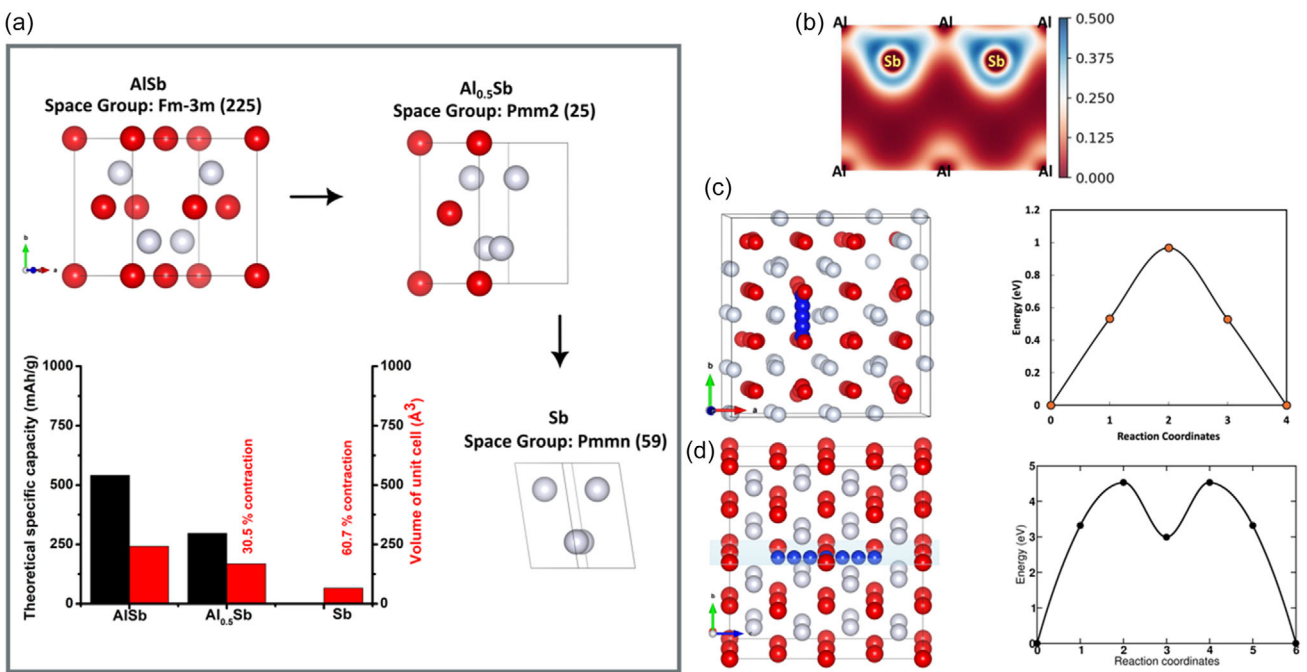


Figure 7. a) possible structural changes during the charging mechanism. Red and silver balls represent Al and Sb atoms, respectively. b) 2D slice of the charge density along the (110) plane of the AlSb. Charge accumulation and depletion regions are represented by the blue and red colors, respectively. c,d) Considered the migration pathway of Al and its corresponding barrier. The migrating Al along the b and c-direction is shown in blue balls.

with bulk metals is: $\Delta E_{disp} = E(AlSb) + E(Ni) - E(NiSb) - E(Al)$, where the displacement exchange reaction is: $NiSb + Al^{3+} + 3e^- \rightarrow AlSb + Ni$. By considering the computational hydrogen electrode and in battery thermodynamics, applying an electrode potential U shifts the electron chemical potential by $-eU$, so any step involving n electrons has $\Delta G(U) = \Delta G(0) - neU$. Electrochemically inserting one Al^{3+} at a cathode potential V changes the free energy roughly as, $\Delta G(V) \approx \Delta E_{disp} - 3\text{ eV}$. Figure 5 shows two cathodic peaks at $\approx 0.46\text{ V}$ and $\approx 0.25\text{ V}$ (vs. Al/AlCl₄⁻) during discharge. We can assign these to sequential alloying steps supported by ex situ XRD Figure S3, Supporting Information and DFT. The higher-voltage cathodic peak ($\approx 0.46\text{ V}$ vs. Al/AlCl₄⁻) corresponds to alloying of Sb with Al to form AlSb, consistent with ex situ XRD and DFT formation energy analysis ($V_{DFT} = 0.11\text{ V}$; $\Delta H_f(AlSb) = -0.34\text{ eV}$). The lower-voltage cathodic peak ($\approx 0.25\text{ V}$) arises from a NiSb-assisted step in which Al insertion converts $NiSb \rightarrow AlSb + Ni$. The 0 K displacement energy for the associated exchange with bulk metals is 0.197 V; the electrochemical driving force reduces this by 3 eV, so the step becomes favorable for $V \gtrsim 0.066\text{ V}$. The observed ≈ 0.25 peak is therefore consistent with a small thermodynamic threshold plus kinetic overpotential. Ex situ XRD after fully Figure S3C, Supporting Information discharged state shows AlSb together with Ni (NiSb suppressed), which matches this sequential assignment.

4.6. Insight into the Capacity Loss

Although the theoretical capacity of the system is 660 mAh g⁻¹, the specific capacity drops to a mere 45 mAh g⁻¹. Wein Gyun

et al. have reported a similar drop in capacity due to the formation of SbCl₅ and SbCl₃ during charging as the reason for capacity degradation; the capacity of the Sb electrode observed in their case was 12 mAh g⁻¹.^[36] Similarly, Jiao et al.^[36] investigated the reaction mechanism of both electrodes and concluded that there was capacity loss (without any modification of separator or electrode) in the aluminum ion batteries could be due to the dissolution of Sb to form SbCl₃ and SbCl₅.

The possibilities of the formation of SbCl₅ and SbCl₃ during charging were investigated through DFT. Formation energies for both SbCl₃ and SbCl₅ were investigated via DFT analysis, and it was found that the formation energy of the SbCl₃ (-3.93 eV) phase is lower in comparison to the SbCl₅ (-1.87 eV). As the electrolyte reacts with the anode when charging, this metastable phase of SbCl₅ could further react with AlCl₃ and produce the stable phase of Al (SbCl₆)₃, which causes severe loss in the specific capacity of the battery. XRD of the charge sample has been performed, which has been shown in Supplementary information Figure S1a, Supporting Information. The XRD spectra show the peak of SbCl₃ in the Sb/Ni electrode at a charged condition. This is completely in accordance with the DFT, as it is more thermodynamically stable as per theoretical analysis.

As Sb turns into SbCl₃ upon charging, two simultaneous events can take place, which may be held responsible for the drop in specific capacity. SbCl₃ is a very low solubility product, and once formed at the positive electrode, it does not dissolve in that electrolyte.^[36] Once SbCl₃ is formed, Al in the next discharge cycle would form AlCl₃, liberating Sb, which would make it intermetallic with Al. This AlCl₃ formation is therefore irreversible, and it exhausts the anode (Al foil) in a cycle with a gradual

drop in capacity. However, this step does not exhaust Sb, as Sb forms $SbCl_3$ during charge and reverts to Sb during discharge. But there can be a loss or dissolution of the main active material, Sb as well, due to the formation of the eutectic, and reaction between the Sb and $SbCl_3$. This will influence the surface/ topology of the electrode as it is cycled. Therefore, to validate this hypothesis, SEM-EDS of the positive Sb electrode in a charged condition (after 50 cycles) has been observed. Along with that, the SEM images of the bare Ni-foam and Sb electrodeposited Ni-foam are also shown for comparison, as shown in the supplementary information Figure S2a-f, Supporting Information.

SEM images of the pristine Ni-foam under 100x and 500x magnifications, as shown in Figure S2a,b, Supporting Information. Both images show porosity with pore diameters in the order of 100–200 μm . Figure S2c,d, Supporting Information show SEM images of as-deposited Sb electrodes under 100x and 500x magnifications. In the morphology, it is found that all the pores of the Ni-scaffold were covered with electrodeposited Sb. Figure S2e,f, Supporting Information show the SEM images of the Sb electrode in a charged state after the 50th electrochemical cycles under 100x and 500x magnifications. In this cycled sample, once again, the porous framework at the base is visible. This means that a large proportion of Sb got converted to $SbCl_3$ while charging, and the remaining portion of Sb reacts with it in the whole reaction procedure and gets dissolved or converted to $AlCl_3$ at discharge, followed by dissolution. The chance under 100x and 500x s of conversion is more, as in charged XRD, peaks of $SbCl_3$ are observed, indicating they have very much less solubility and are less likely to dissolve directly in the electrolyte. Rather, this insoluble $SbCl_3$ during discharge converts to $AlCl_3$ and dissolves in the electrolyte, creating pores/holes in the electrode structure. Al then reacts with the Sb (liberated from $SbCl_3$ due to the formation of $AlCl_3$) and exhibits electrochemical capacity by the formation of AlSb intermetallic. However, due to this irreversible loss of Al (due to the formation and dissolution of $AlCl_3$ as well as Sb at the cathode), the capacity keeps on decreasing till the electrolyte becomes saturated with $AlCl_3$, inhibiting the dissolution process.

5. Conclusion

In this work, Sb was utilized as the positive electrode to fabricate an aluminum intermetallic battery. Aluminum during discharge forms AlSb intermetallic at 0.45 V (w.r.t. Al/ Al^{3+}) and during charge, the intermetallic dissociates with aluminum plating back to its pristine condition. Ni-foam is used as the current collector for Sb to buffer the volumetric expansion due to the formation of AlSb. At a current density of 100 mA g^{-1} , the discharge capacity exhibited $\approx 81\text{ mAh/g}$ on average with a second-cycle specific capacity of 74 mAh g^{-1} . However, after 50 cycles, the electrode exhibited a specific capacity of merely 22 mAh g^{-1} . Here, the capacity retention rate (28%) is higher without any modification in the current collector or in the separator, which is due to the structural stability and mechanical integrity of the 3D porous Ni-foam collector. But the dissolution of active material is a crucial factor; if this issue of capacity retention is

addressed, the Al-Sb intermetallic cell (with Ni-foam as current collector) has the potential to emerge as a grid-scale stationary battery due to the abundance of low-cost ingredients. The main objective of this work was to validate the Al intermetallic reaction through the galvanic cell mechanism, as well as the superiority and utilization of the Ni-foam as a current collector without any modification. The cell can also be further modified by eliminating the parasitic side reactions in the future.

Acknowledgements

This work was supported by the Indian Institute of Technology Jodhpur under the seed-grant scheme I/SEED/SSG/20210025, R/I/SEED/PRJ/DSN/AB/20220044, and by the DST-SERB R/S/SERB/AB/20220081.

Conflict of Interest

The authors declare no conflict of interest.

Data Availability Statement

The data that support the findings of this study are available from the corresponding author upon reasonable request.

Keywords: Al-based rechargeable battery · antimony- cathode · intermetallic batteries · ni-foam current collector

- [1] M. Fichtner, K. Edström, E. Ayerbe, M. Berecibar, A. Bhowmik, I. E. Castelli, S. Clark, R. Dominko, M. Erakca, A. A. Franco, A. Grimaud, B. Horstmann, A. Latz, H. Lorrmann, M. Meeus, R. Narayan, F. Pammer, J. Ruhland, H. Stein, T. Vegge, M. Weil, *Adv. Energy Mater.* **2022**, *12*, 2102904.
- [2] A. Dey, G. Varshney, S. Halder, A. D. Singh, A. Cyril, A. Banerjee, S. Sengupta, *J. Power Sources* **2025**, *656*, 238034.
- [3] Z. Wang, Y. Li, Q. Zhou, Q. Li, R. Zhao, Z. Qiu, R. Zhang, Y. Sun, F. Wu, C. Wu, Y. Bai, *Energy Mater. Adv.* **2024**, *5*, 1.
- [4] N. Kamboj, A. Dey, S. Birara, M. Majumder, S. Sengupta, R. K. Metre, *Dalton Trans.* **2024**, *53*, 7152.
- [5] A. Dey, S. Goswami, S. N. Das, D. Bhattacharya, C. K. Ghosh, *Phys. B Condens. Matter* **2023**, *667*, 415207.
- [6] J. M. Tarascon, M. Armand, *Nature* **2001**, *414*, 359.
- [7] W. Guo, X. Xue, S. Wang, C. Lin, Z. L. Wang, *Nano Lett.* **2012**, *12*, 2520.
- [8] A. D. Singh, A. A. Cyril, G. Varshney, A. Dey, S. Sengupta, *J. Alloys Compd.* **2024**, *1005*, 176174.
- [9] F. Wu, *Energy Mater. Adv.* **2025**, *6*, 1.
- [10] Q. Zhao, Y. Lu, J. Chen, *Adv. Energy Mater.* **2017**, *7*, 1601792.
- [11] N. Jayaprakash, S. K. Das, L. A. Archer, *Chem. Commun.* **2011**, *47*, 12610.
- [12] G. A. Elia, K. Marquardt, K. Hoeppner, S. Fantini, R. Lin, E. Knipping, W. Peters, J. F. Drillet, S. Passerini, R. Hahn, *Adv. Mater.* **2016**, *28*, 7564.
- [13] L. Wang, F. Liu, W. Wang, G. Yang, D. Zheng, Z. Wu, M. K. H. Leung, *RSC Adv.* **2014**, *4*, 30857.
- [14] H. Sun, W. Wang, Z. Yu, Y. Yuan, S. Wang, S. Jiao, *Chem. Commun.* **2015**, *51*, 11892.
- [15] H. Wang, Y. Gao, Y. Li, H. Yang, W. Liu, B. Long, F. Wu, Y. Bai, C. Wu, *Energy Mater. Adv.* **2024**, *5*, <https://doi.org/10.34133/energymatadv.0117>.
- [16] M. C. Lin, M. Gong, B. Lu, Y. Wu, D. Y. Wang, M. Guan, M. Angell, C. Chen, J. Yang, B. J. Hwang, H. Dai, *Nature* **2015**, *520*, 324.
- [17] W. Wang, B. Jiang, W. Xiong, H. Sun, Z. Lin, L. Hu, J. Tu, J. Hou, H. Zhu, S. Jiao, *Sci. Rep.* **2013**, *3*, 1.
- [18] T. Zhao, M. Ojeda, J. Xuan, Z. Shu, H. Wang, *Energy Procedia* **2019**, *158*, 4829.

- [19] S. Wang, S. Jiao, J. Wang, H. Sen Chen, D. Tian, H. Lei, D. N. Fang, *ACS Nano* **2017**, *11*, 469.
- [20] G. Cohn, L. Ma, L. A. Archer, *J. Power Sources* **2015**, *283*, 416.
- [21] W. Simka, D. Puszczynk, G. Nawrat, *Electrochim. Acta* **2009**, *54*, 5307.
- [22] T. Jiang, M. J. Chollier Brym, G. Dubé, A. Lasia, G. M. Brisard, *Surf. Coat. Technol.* **2006**, *201*, 10.
- [23] T. Jiang, M. J. Chollier Brym, G. Dubé, A. Lasia, G. M. Brisard, *Surf. Coat. Technol.* **2006**, *201*, 1.
- [24] S. Mohapatra, S. Halder, S. R. Chaudhari, R. R. Netz, S. Mogurampelly, *J. Chem. Phys.* **2023**, *159*, 154902.
- [25] P. Kumar, S. Mohapatra, S. Halder, S. Mogurampelly, *J. Mol. Liq.* **2024**, *397*, 124159.
- [26] G. Varshney, A. Dey, A. D. Singh, A. A. Cyril, P. Ranjan, S. Sengupta, *J. Alloys Compd.* **2025**, *1014*, 178692.
- [27] H. Yang, F. Wu, W. Liu, X. Wang, Y. Bai, C. Wu, *Energy Storage Mater.* **2022**, *51*, 435.
- [28] H. Liu, S. Wang, J. Zhao, B. Zhang, L. Liu, R. Bao, Z. Jing, *J. Energy Storage* **2024**, *80*, 109862.
- [29] A. D. Singh, A. A. Cyril, A. Dey, G. Varshney, S. Sengupta, *J. Alloys Compd.* **2024**, *977*, 173305.
- [30] A. Chaupatnaik, P. Barpanda, *Electrochim. Commun.* **2021**, *127*, 107038.
- [31] M. Martos, J. Morales, L. Sánchez, *Electrochim. Acta* **2003**, *48*, 615.
- [32] X. Yang, J. P. A. Wärnå, J. Wang, P. Zhang, W. Luo, R. Ahuja, *J. Catal.* **2021**, *404*, 18.
- [33] H. J. Monkhorst, J. D. Pack, *Phys. Rev. B* **1976**, *13*, 5188.
- [34] H. Jonsson, G. Mills, K. W. Jacobsen, *Nudged Elastic Band Method for Finding Minimum Energy Paths of Transitions*, **1998**, 385–404.
- [35] G. Henkelman, H. Jónsson, *J. Chem. Phys.* **2000**, *113*, 9978.
- [36] W. Guan, L. Wang, J. Tu, S. Jiao, *J. Electrochem. Soc.* **2020**, *167*, 080541.

Manuscript received: July 5, 2025

Revised manuscript received: August 16, 2025

Version of record online: